

Analysis of Unsteady Airfoils at Low Speeds

X. Bertrán[◇], H. Olivier[◇], S. Turek[‡]

[◇] Shock Wave Laboratory

Aachen University of Technology, Germany

[‡] Institute for Applied Mathematics, LS III

University of Dortmund, Germany

Summary

In this study exemplary results on the influence of two fundamental unsteady parameters, the reduced frequency k and the non-dimensional pitching rate α_+ , on the transition from a steady to an unsteady flow field around the reference airfoil BAC3-11/RES/30/21 are presented using experimental and numerical techniques. The tools used are described and their results verified with each other. On the experimental side, water tunnel experiments are conducted using particle-image-velocimetry (PIV) and strain-gauge-balance (SGB) measurement techniques. The experimental results are enhanced by two-dimensional laminar unsteady numerical Navier-Stokes simulations of the experiments with a state of the art code from the Featflow package. The numerical simulations are found to agree well with experimental results, despite three-dimensional effects and a relatively high Reynolds number of $Re_c = 16000$. An influence of the reduced frequency on the lift coefficient at a local non-dimensional pitching rate value of $\alpha_+ = 0$ for the relevant range is not detected, while for the drag and the pitching moment a decrease and an increase respectively is observed. Nevertheless a phase difference for the lift with increasing reduced frequency was calculated, which appears at least above $k = 0.14$ and indicates unsteady effects. The same was observed for the pitching moment. The effects of the airfoil camber are clearly seen during the phase of negative angle of attack, inducing leading and trailing edge separation. The flow separation regions are discussed and the formation of a triple vortex system at the trailing edge in the pitching up motion of the airfoil is identified in the experimental and numerical data.

1 Introduction

In the past decade aeroelasticity has been playing a fundamental role in the development of new aircraft for various reasons and new tools have been de-

signed to speed up the development process [1, 2]. While reliable tools for on-design conditions exist, there is a lack of tools for off-design conditions, where in most cases unsteady flow fields are encountered. Even though there have been numerous studies in this field for special cases such as dynamic stall, still many flow field conditions have not been explored. Especially the transition process from a quasi-steady to an unsteady flow field has only seldom been analyzed. An attempt is to be made in this study using experimental and numerical techniques available.

By definition a time varying flow field is unsteady, but there are situations where a time dependent flow field can be considered steady, thus quasi-steady. For example in the case of flutter, the initial situation may be a steady flow field, which due to increasing unsteady effects and airfoil motion, becomes unsteady. It therefore goes through a transition process from a steady to an unsteady flow field. To study this process, the model problem - the oscillating thin airfoil - is used, which has been thoroughly analyzed in the past [3]. In general the unsteady motion of oscillating thin airfoils is characterized by the reduced frequency k , which represents the ratio between the time a particle takes to pass the chord length and the time of an oscillation cycle. As the reduced frequency decreases the flow field becomes increasingly steady. The aim is to determine the influence of the reduced frequency and other parameters in the transition process from a steady to unsteady flow.

2 The Facility and Measurement Techniques

2.1 Water-Ludwig-Tunnel

The Water-Ludwig-Tunnel is a short duration facility for the study of unsteady hydrodynamic phenomena, which was proposed by Akamatsu in 1978 [4]. The principle is shown schematically in Fig. 1. The Water-Ludwig-Tunnel is divided in two parts, a high and a low pressure section, thereby resembling a shock tube set-up. Both are separated by a pneumatically driven fast acting valve with a very short opening time ($\approx 9\text{ ms}$). The high pressure section is divided into three parts, the top being the storage tank followed by the nozzle and the test section. The test section is 150 mm wide and 75 mm deep and has a length of about 820 mm . The test section ends in the fast acting valve, consisting of a perforated flat plate connected to the rod of a pneumatic actuator. The valve opening ratio Kv can be adjusted to give the desired free stream velocity u_∞ in the test section. The low pressure section consists of the retainment tank and a water pump, which is connected to the storage tank and a water supply. The facility can either be controlled manually or by a PC. Models are mounted onesided and 0.280 m away from the nozzle exit in the test section. The model investigated here is the reference

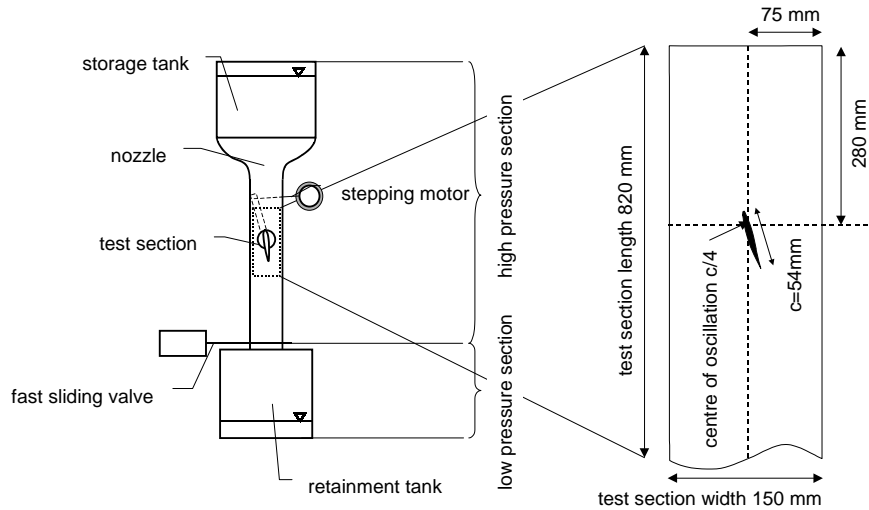


Figure 1 Schematic view of the Water-Ludwig-Tunnel

airfoil BAC3-11/RES/30/21 with a chord length of 54 mm of the collaborative research center SFB 401 "Flow Control and Fluid-Structure Interaction at Airplane Wings". The measurement techniques applied are:

- digital flow visualization via particle tracking,
- digital Particle-Image-Velocimetry (PIV),
- and the measurement of forces and the pitching moment with a three-component strain gauge balance.

2.2 Particle-Image-Velocimetry (PIV) and Flow Visualization

2.2.1 PIV-system

This PIV-system was designed to examine oscillating airfoils in an unsteady water flow. In the past, problems accounted to phase averaging methods used to analyze unsteady flow fields have been reported (see [5]). At the same time Wernert et al. [6] have demonstrated, that vector plots from several oscillations go aside with having non-reproducible results concerning the unsteady flow field of an airfoil in deep stall. Therefore the main aim for this PIV-system was to extract 10 vector plots from one single oscillation, in order to attain as much information as needed to examine the unsteady behaviour of the flow without having to use phase averaging methods or to

assemble PIV-recordings from several oscillations. The number of oscillations is restricted by the short testing time in the Water-Ludwig-Tunnel, making it impossible to employ phase averaging techniques with accuracy. The recording technique was kept as simple as possible, but at the same time able to generate high resolution pictures by using a digital CCD-camera. A digital recording was favoured to reduce postprocessing time. For a detailed description of the fundamentals concerning the PIV-technique, the reader is referred to [7, 8, 9]. Here a short overview of the underlying methods used in this PIV-system will be given. In PIV, a laser beam is expanded into a

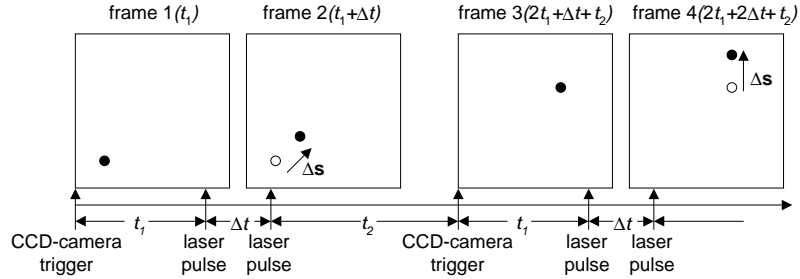


Figure 2 Single pulse multi-frame mode operation of the PIV-system

light sheet and is introduced into the flow seeded with particles (see Fig. 3). The light is scattered by the particles and can be recorded perpendicular to the plane of the light sheet. In this case a CCD-camera is used to record two sequential frames a Δt apart of the flow field. The frames contain images of particles suspended in the flow, which are chosen in a way so that they follow the local flow as accurately as possible. The displacement can therefore be calculated by:

$$\mathbf{u} = \frac{\Delta \mathbf{s}}{M \Delta t}. \quad (1)$$

Where M is the magnification. For these studies highly unsteady flow fields were expected, therefore only a recording of multiple single exposure frames was considered which also has the advantage of removing directional ambiguity encountered using multiple exposure frames, illustrated in Fig. 2. In this mode the analysis is performed using cross-correlation [9, 10]. For this purpose the frames are divided into subspaces called interrogation regions 32×32 or 64×64 *Pixels* wide. The spacing between the interrogation regions is varied from 50% to 75% overlap respectively. Cross-correlation requires a sufficient number of particles $N > 10 - 20$ in the interrogation region. The laser pulse length is $200 \mu s$ and laser pulse separation is $1000 \mu s$.

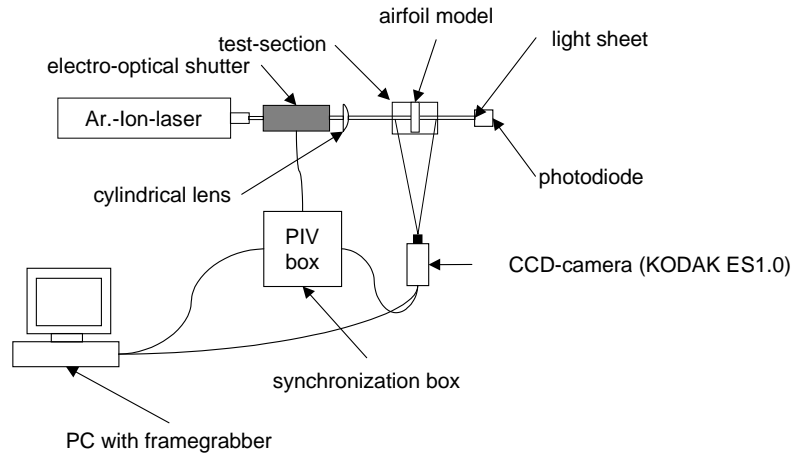


Figure 3 A view of the PIV system

Illumination

Illumination is achieved by using a continuous wave Argon-ion laser model Spectra-Physics 2000-05 with a maximum power output of 5 Watts in multi-line mode. The laser power during experiments was adjusted to be typically between 2.5 – 4.2 W. The laser aperture was opened at its maximum and was directed straight at the test section to have its full power available. The laser beam is aligned with an electro-optical shutter of type Dantec/Invent 80x41, a cylindrical lens and a vertical aperture to create a light sheet with a thickness of 2 mm.

Particles

Vestamid 1111 particles are used which have a diameter of about 100 μm . Seeding is done manually by measuring the volume of the particles about to be dispensed in the water ($\sim 150 ml$). The density is a little lower than that of water. It is therefore inevitable to run the test water several times through the facility in order to have a homogeneous seeding. The size of the particles is chosen to give an approximate particle image on the CCD-chip of 1 – 3 pixels, depending on the size of the flow region recorded.

Evaluation

The PIV-system was evaluated by measuring the velocity in the empty test-section and comparing the results with Laser-doppler-anemometry used to

measure the free-stream velocity. The mean error is roughly 2%, which is the overall error to be expected from such a system. Figure 4 shows the values plotted against each other and a good agreement can be found.

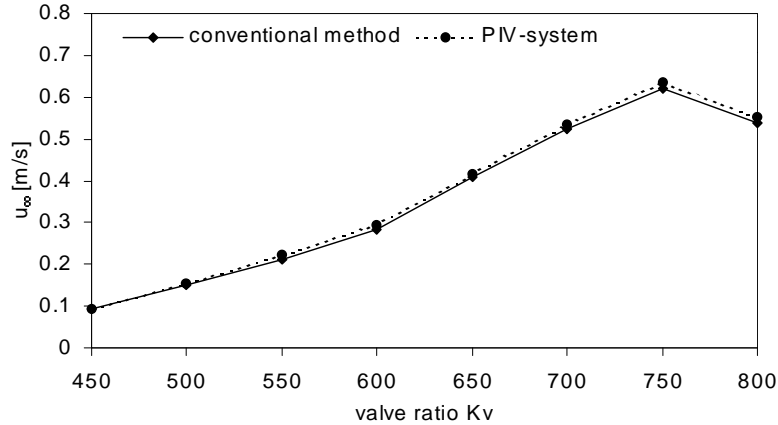


Figure 4 Comparison of the free-stream velocity measured by the PIV-system with the conventional method (LDA)

2.2.2 Flow Visualization

Digital visualization is achieved by recording the particles illuminated by a light sheet in the mid-section of the test section with a CCD Camera. The same device is a component of the PIV-system installed. Exposure times are 15 *ms* to generate relatively long particle lines in order to compare them well with numerical data visualization. Total frame time is 32 *ms* allowing for a good contrast and the frame rate is 10 *Hz*.

2.3 Strain-Gauge-Balance (SGB)

The three-component strain-gauge-balance is constructed out of commercially available load cells. Figure 5 shows the setup of the strain-gauge-balance. The load cell section is sealed by a rubber bellow reaching from the model mount to the back flange. The influence of the rubber bellow in constant pressure conditions is negligible, while for varying pressure conditions the measured values have to be corrected. It measures the normal and axial forces and the pitching moment in strain-gauge-balance coordinates (SGB), which are rotated relatively to the model coordinate system (AM) in order to optimize the actual force components acting in the load cell direction. The

pitching moment is equal in all coordinate systems. The aerodynamic forces in the aerodynamic coordinate system are given by:

$$\begin{aligned} L &= N_{SGB} \cos(\varepsilon - \alpha) + T_{SGB} \sin(\varepsilon - \alpha) \\ D &= -N_{SGB} \sin(\varepsilon - \alpha) + T_{SGB} \cos(\varepsilon - \alpha), \end{aligned} \quad (2)$$

where ε is equal to 45° and α is the angle of attack. During the post-processing the signals are transformed and filtered to erase noise and vibrational influences occurring during the measurement. The forces acting on the SGB are very small and in the order of $\sim 10^{-1} N$ and the pitching moment even smaller in the order of $\sim 10^{-4} Nm$. Therefore force and moment measurements have to be taken with care as they are easily influenced by external laboratory vibrations.

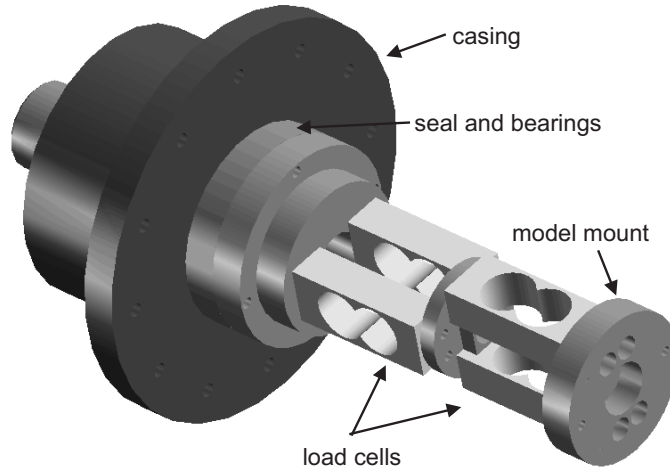


Figure 5 Schematic view of the strain-gauge-balance

2.4 Experimental Conditions

The experiments in this study were performed with the test section conditions in Tab. 1. The kinematic parameters of the model pitching motion were varied according to Tab. 2. The Reynolds number was chosen to suppress the generation of turbulence while at the same time generating enough force and moment for the strain-gauge-balance to measure properly. Lower reduced frequencies are not possible in the experiments, as the minimum number of oscillations was set to 2 in the available time.

Table 1 Experimental conditions in the test section

Description	Variable	Value
Free-stream velocity	u_∞	0.3 m/s
Characteristic acceleration time	τ	~ 17 ms
Deceleration	$\frac{\partial u}{\partial t}$	0.0032 m/s ²
Model Reynolds number	Re_c	16000

Table 2 Kinematic parameters of the model motion

Description	Variable	Value
Mean angle of attack	α_M	0°
Amplitude angle of attack	α_A	3 and 6°
Frequency	f	0.25, 0.3, 0.35, 0.4, 0.45 and 0.5 Hz
Reduced frequency	k	0.14 – 0.28

3 Numerical Techniques

3.1 The Navier-Stokes Solver

The modified flow code PP2DMOV solves the unsteady 2-dimensional Navier-Stokes equations in an Arbitrary Lagrangian-Eulerian (ALE) formulation on a region Ω . It essentially is based on the discrete projection type solver PP2D from the FEATFLOW package, which was modified to simulate incompressible two-dimensional flows with moving boundaries in an efficient way. Here only a short description will be given of the PP2D solver. For a detailed description of the numerical background the reader is referred to [11, 12]. The incompressible Navier-Stokes equations can be given by:

$$\begin{aligned} \frac{\partial u}{\partial x} + \frac{\partial v}{\partial y} &= 0 \\ \rho \frac{\partial u}{\partial t} + \rho \left(u \frac{\partial u}{\partial x} + v \frac{\partial u}{\partial y} \right) &= \rho \nu \left(\frac{\partial^2 u}{\partial x^2} + \frac{\partial^2 u}{\partial y^2} \right) - \frac{\partial P}{\partial x} + f_x \\ \rho \frac{\partial v}{\partial t} + \rho \left(u \frac{\partial v}{\partial x} + v \frac{\partial v}{\partial y} \right) &= \rho \nu \left(\frac{\partial^2 v}{\partial x^2} + \frac{\partial^2 v}{\partial y^2} \right) - \frac{\partial P}{\partial y} + f_y. \end{aligned} \quad (3)$$

Using $p = \frac{P}{\rho}$, they can be written in a more compact form:

$$\mathbf{u}_t - \nu \Delta \mathbf{u} + \mathbf{u} \cdot \nabla \mathbf{u} + \nabla p = \mathbf{f}, \quad \nabla \cdot \mathbf{u} = 0, \quad \text{in } \Omega \times [0, T]. \quad (4)$$

Equation 4 is solved by first introducing a time discretization, in this case the robust Fractional-step- θ -scheme which is of second order accuracy. In

general form in each time step the following Quasi-Navier-Stokes problems are solved:

Given \mathbf{u}^n and the time step $k = t_{n+1} - t_n$, then solve for $\mathbf{u} = \mathbf{u}^{n+1}$ and $p = p^{n+1}$

$$\frac{\mathbf{u} - \mathbf{u}^n}{k} + \theta [-\nu \Delta \mathbf{u} + \mathbf{u} \cdot \nabla \mathbf{u}] + \nabla p = \mathbf{g}^{n+1} \quad , \quad \nabla \cdot \mathbf{u} = 0, \quad (5)$$

with the right hand side

$$\mathbf{g}^{n+1} = \theta \mathbf{f}^{n+1} + (1 - \theta) \mathbf{f}^n - (1 - \theta) [-\nu \Delta \mathbf{u}^n + \mathbf{u}^n \cdot \nabla \mathbf{u}^n] \quad (6)$$

The parameter θ is chosen according to the time step scheme used. Discretization in space is achieved by using finite elements. Starting from a variational formulation, the region Ω is divided by a finite mesh of quadrilaterals, where trial functions for velocity and pressure are defined. The quadrilateral used in PP2DMOV uses nonparametric piecewise rotated bilinear shape functions for the velocities spanned by $\langle x^2 - y^2, x, y, 1 \rangle$ and piecewise constant pressure approximations. This gives us an element where the velocities are defined as mean nodal values on the element edges with a cell-centered nodal value for the pressure. In finite element terms this element pair $\tilde{Q}1/Q0$ is non-conforming. The non-linear 1-step projection solution process is accelerated with a multigrid technique. PP2D has successfully taken part in the DFG-Benchmark Computation within the DFG priority Research Program "Flow Simulation on High Performance Computers" [13].

To provide a little insight to the solution process commonly used in PP2D and hence in PP2DMOV, the nonlinear 1-step projection scheme will be presented in the following section. Again, for detailed information on the algorithms and approaches used, the reader is referred to [12].

Nonlinear 1-step projection scheme:

Given: Iterates $\mathbf{u}^{n-1} = \mathbf{u}(t_{n-1})$ and $p^{n-1} = p(t_{n-1})$ from time level $n - 1$

Perform: 5 sub-steps to obtain \mathbf{u}^n and p^n on the new time level n

1. Solve for an intermediate velocity $\tilde{\mathbf{u}}^n$ the corresponding nonlinear momentum equation. The right hand side has the vector of time level t_n and the last gradient of the pressure p^{n-1} ,
2. Solve a pressure-poisson problem for a right hand side f_p with the divergence from $\tilde{\mathbf{u}}$,
3. Update the pressure by additionally applying a diffusive preconditioner,
4. Finally update the new velocity \mathbf{u}^n to satisfy the continuity equation.

PP2DMOV is basically just an extension of PP2D by introducing the mesh velocity in the convective term of the incompressible two-dimensional Navier-Stokes equations (see Eq. 7). In the literature this is referred to as an Arbitrary Lagrangian-Eulerian (ALE) formulation. Note that mesh velocities \mathbf{u}_G do not appear in the continuity equation, as a pressure-poisson equation is solved to satisfy the continuity equation in an outer loop. Care has to be taken to satisfy the geometric conservation law (GCL), where the mesh velocity \mathbf{u}_G must be equal to the movement of the mesh $\Delta \mathbf{x}$ during the time step k .

$$\mathbf{u}_t - \nu \Delta \mathbf{u} + (\mathbf{u} - \mathbf{u}_G) \cdot \nabla \mathbf{u} + \nabla p = \mathbf{f}, \quad \nabla \cdot \mathbf{u} = 0, \quad \text{in } \Omega \times [0, T]. \quad (7)$$

The following modifications were performed on PP2D:

- auxiliary routines to update the matrices in every sub time step according to the new position of mesh nodes,
- handling of meshes, such as interpolation and a local refinement process in the vicinity of boundaries,
- and changes in the upwinding scheme to satisfy the GCL.

No changes were made in algorithmic solution process. An update of the corresponding matrices according to the new mesh position is performed, allowing a very efficient time dependent handling of the mesh and the corresponding boundary conditions.

3.2 Moving Mesh

3.2.1 Mesh Interpolation

In order not to change the algorithmic approach of PP2D, the mesh is refined for the multigrid driver in every sub-step of the time scheme used. Therefore changes to the mesh are applied at coarse grid level only, before all other levels are created. This procedure is certainly not optimal in respect to the computational cost, but leaves many possibilities for moving the mesh. The method used in this study is very simple and uses blending functions to interpolate a mesh between two fixed positions, the original and the rigidly transformed mesh, in this case a rotation about the 1/4 chord point of the airfoil for a given angle of attack. The blending functions are constructed as polynomials and use the closest distance to the boundaries as input. The method is derived from [14], where it has been successfully used for structured grids. Figures 6 and 7 show the original and the resulting rotated mesh for an angle of attack of 6° . Mesh deformations without cross-overs up to large angles of attack of 40° are possible using this method. The elements near to the airfoil are moved nearly rigidly with the airfoil in order to preserve the quality of the mesh in these regions.

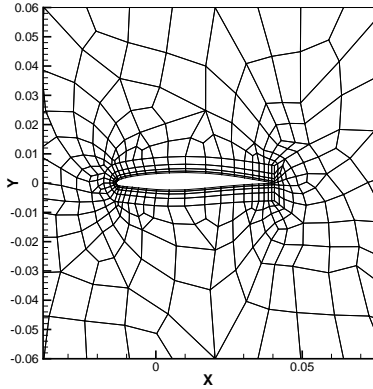


Figure 6 Coarse mesh at $\alpha = 0^\circ$

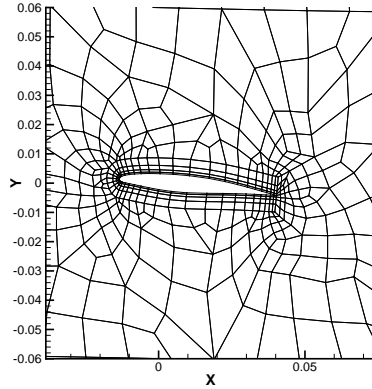


Figure 7 Coarse mesh at $\alpha = 6^\circ$

3.2.2 Boundary Mesh Refinement

Normally, the mesh in the FEATFLOW solvers is refined for the multigrid driver with a common $h/2$ refinement, which means that a quadrilateral is refined into four new elements using the midpoints of the edges and the cell-centered node. Using such a refinement with the interpolation method would result in a poor spatial resolution of the boundary layers. Therefore

the refinement strategy was modified to resolve this problem. A coefficient, which can be chosen by the user, determines the position of the new points on the edges attached to boundaries creating the new four elements. Figure 8 illustrates the process. The spacing Δs between the node on the boundary and the first node in the flow can be given by:

$$\Delta s_{N_L} = c_B^{(N_L - N_{L_{MIN}})} \cdot \Delta s_{N_{L_{MIN}}}, \quad (8)$$

where c_B is a constant factor smaller than 0.5. Equation 8 can also be used to incorporate an adaptive refinement for each edge, where the distance Δs_{N_L} is given and c_B is calculated accordingly.

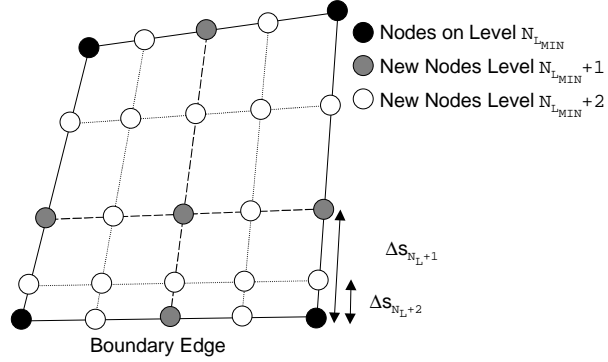


Figure 8 Boundary mesh refinement strategy to resolve boundary layers

3.2.3 GCL and the Upwind Scheme

Weighted Samarski upwinding is used for PP2DMOV, where the mesh velocities \mathbf{u}_G are subtracted and calculated according to the nodal movement from the previous time step, thus satisfying the geometric conservation law automatically [15]:

$$\mathbf{u}_G = \frac{1}{k} \begin{pmatrix} x^{n+1} - x^n \\ y^{n+1} - y^n \end{pmatrix}. \quad (9)$$

Where k is the time step size and n denotes the time step number. The correct implementation was tested on a classic driven cavity problem with a moving mesh.

3.3 Boundary Conditions

The following boundary conditions are prescribed for the simulations concerning the Water-Ludwig-Tunnel [16]. At the inflow section, Dirichlet boundary

conditions are applied, setting the velocity as a function of time:

$$u(t) = u_\infty \tanh\left(\frac{t}{\tau}\right) + kt, \quad v(t) = 0. \quad (10)$$

k is the deceleration factor, when the water level starts to drop in the storage tank of the Water-Ludwig-Tunnel. There are no slip boundary conditions at the upper and lower tunnel wall (see Fig. 9). On the model boundary,

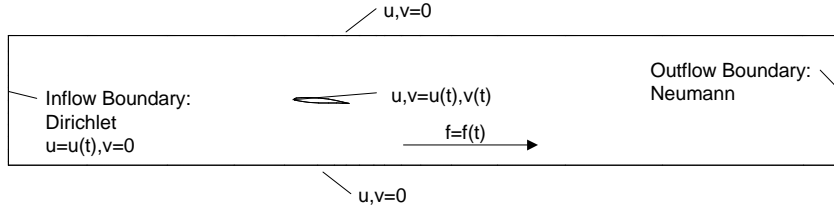


Figure 9 Boundary conditions applied to numerical simulations of Water-Ludwig-Tunnel experiments

the model rotation about a fixed point (x_M, y_M) is differentiated to give the velocities for the Dirichlet boundary condition given in Eq. 11. Thus if no motion is prescribed (i.e. fixed angle of attack), no slip boundary conditions apply to the model.

$$\begin{aligned} \alpha(t) &= \alpha_M + \alpha_A \sin(2\pi f(t - t_{osc})), \\ \dot{\alpha}(t) &= 2\pi f \alpha_A \cos(2\pi f(t - t_{osc})), \\ u(t) &= \dot{\alpha}(y(t) - y_M), \\ v(t) &= -\dot{\alpha}(x(t) - x_M). \end{aligned} \quad (11)$$

Further, a force acts on the fluid derived from Eq. 10 for which the acceleration must be set on the right hand side of the Navier-Stokes equations in Eq. 3 to:

$$f_x = \frac{u_\infty}{\tau} \left[1 - \left(\tanh\left(\frac{t}{\tau}\right) \right)^2 \right] + k, \quad f_y = 0. \quad (12)$$

3.4 Verification of the Numerical Techniques

The correct simulation of experiments with PP2DMOV is verified with experimental data. It must be emphasized that the numerical simulation is performed in a two-dimensional space whereas the experiments are carried out in three dimensions. Therefore the numerical simulation does not account for three-dimensional effects such as side wall interference in form of

a horse-shoe vortex, corner vortices and many others. The small aspect ratio of the model (~ 1.4) certainly does not improve the situation. Despite these set-backs a good agreement between numerical and experimental data is found, sufficient to enhance experimental results and give a greater insight into the occurring flow phenomena.

3.4.1 BAC3-11 at $\alpha_M = 6^\circ$, $\alpha_A = 0^\circ$ and $f = 0 \text{ Hz}$

In this case of a static airfoil the time dependent flow phenomena are initialized by the impulsive start of the flow in the tunnel (see Eq. 10). In Figs. 10 and 11 the experimental and numerical aerodynamic coefficients are plotted versus time and a reasonable agreement can be observed, except for the dynamic effects in the first second. The trailing edge separation bubble leads to a break in the development of the aerodynamic lift. The breaking point in the form of a peak at about 0.5 s cannot be clearly detected in the experimental values. From one second onwards a good agreement is found, where three-dimensional effects can be clearly detected in the experimental lift signal as trailing edge vortex shedding is disturbed in comparison with numerical data. The mean steady aerodynamic lift and drag values agree reasonably. The mean pitching moment coefficient is slightly smaller, but as mentioned earlier pitching moment results at these conditions have to be taken with care as the order of magnitude is very small. Nevertheless the frequency of the vortex shedding process is equal in both cases. A compari-

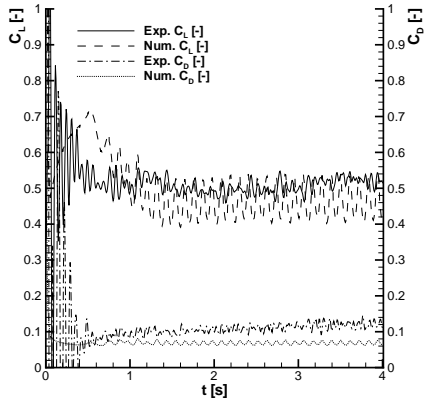


Figure 10 Lift and drag coefficients from experimental and numerical data for $\alpha_M = 6^\circ$, $\alpha_A = 0^\circ$ and $k = 0$

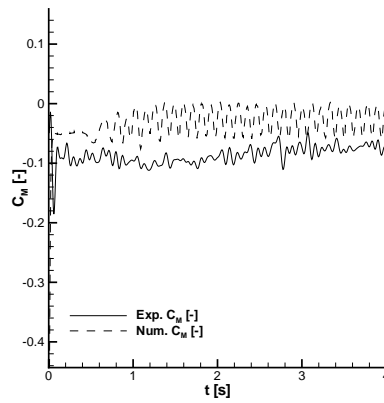


Figure 11 Pitching moment coefficient from experimental and numerical data for $\alpha_M = 6^\circ$, $\alpha_A = 0^\circ$ and $k = 0$

son of instantaneous streamlines and flow visualization reveals a good overall agreement. Figures 12 and 13 show a good agreement of the flow phenomena

encountered exactly at $t = 0.6$ s. Especially the primary trailing edge vortex can be identified and is also situated in the same position relative to the airfoil. The boundary layer separation point on the upper side also coincides. In Figs. 14 and 15 a triple vortex structure can be observed in both cases, revealing a very good agreement between experiment and numerical simulation. The laminar separation point has moved upstream in comparison with the flow at $t = 0.6$ s. Comparing numerical results with PIV data also shows a good agreement (Figs. 16 and 17). Two vortices can be observed in the PIV and numerical data at nearly the same relative position to the airfoil.

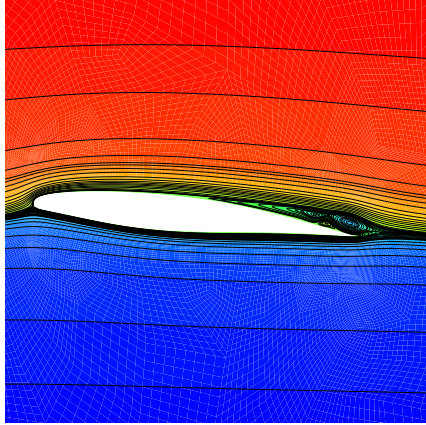


Figure 12 Numerical instantaneous streamlines at $\alpha = 6^\circ$ and $t = 0.601$ s for $\alpha = 6^\circ$ and $k = 0$

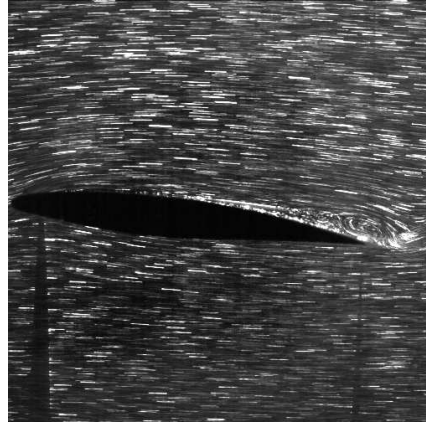


Figure 13 Experimental particle visualization at $\alpha = 6^\circ$ and $t = 0.6$ s for $\alpha_M = 6^\circ$, $\alpha_A = 0^\circ$ and $k = 0$

3.4.2 BAC3-11 at $\alpha_M = 0^\circ$, $\alpha_A = 6^\circ$ and $f = 0.25$ Hz

After discovering a good agreement at a fixed angle of attack, it is necessary to verify the agreement at a varying angle of attack. For this purpose the experiment with the lowest reduced frequency was chosen and it must be noted that the same agreement can be found for higher reduced frequencies. In Figs. 18 and 19 both numerical and experimental aerodynamic coefficients are plotted against time, revealing a reasonable agreement. The pitching moment coincides well, except for some peaks. The lift coefficient agrees, except for negative peak values of the angle of attack, where the vortices on the lower side (see Fig. 22) seem to create an extra peak in the lift and pitching moment. This is probably due to an inhomogeneous vortex field in spanwise direction for which the three-dimensional integration of the forces and the pitching moment by the strain-gauge-balance damps out the effect so that they are not detected in the signal. The mean drag coefficient falls short

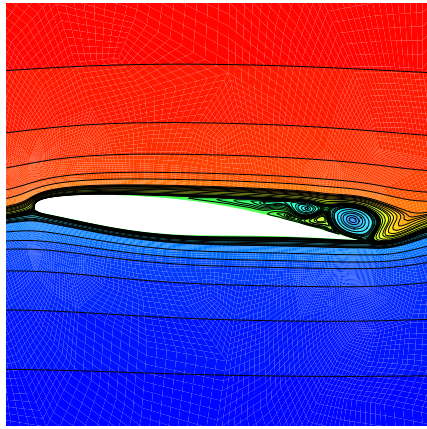


Figure 14 Numerical instantaneous streamlines at $\alpha = 6^\circ$ and $t = 1.204$ s for $\alpha_M = 6^\circ$, $\alpha_A = 0^\circ$ and $k = 0$

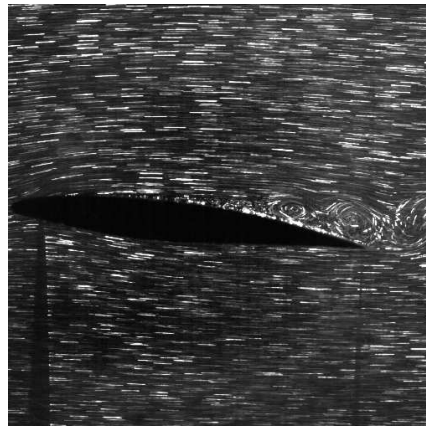


Figure 15 Experimental particle visualization at $\alpha = 6^\circ$ and $t = 1.2$ s for $\alpha_M = 6^\circ$, $\alpha_A = 0^\circ$ and $k = 0$

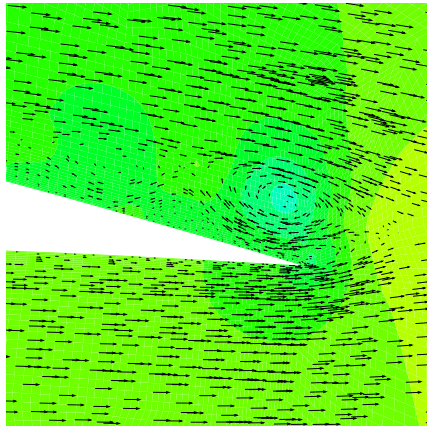


Figure 16 Numerical vectors at $\alpha = 6^\circ$ and $t = 1.204$ s for $\alpha_M = 6^\circ$, $\alpha_A = 0^\circ$ and $k = 0$

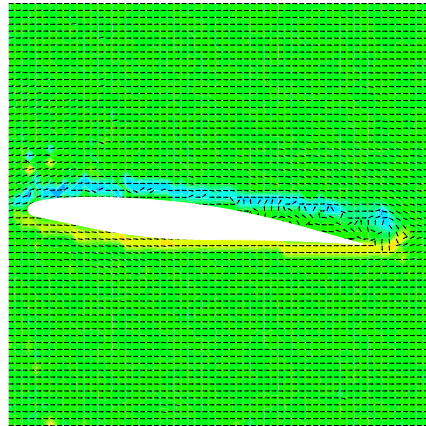


Figure 17 Experimental vectors from PIV at $\alpha = 6^\circ$ and $t = 1.2$ s for $\alpha_M = 6^\circ$, $\alpha_A = 0^\circ$ and $k = 0$

of the experimental values, but has the same appearance in time. Figures 20

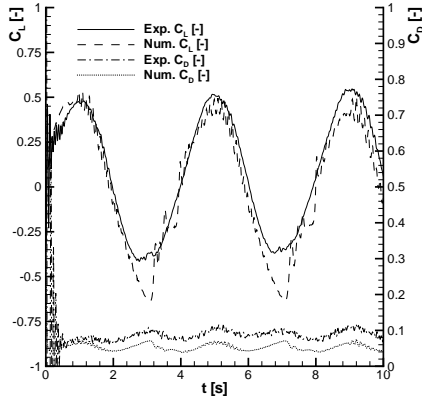


Figure 18 Lift and drag coefficients from experimental and numerical data for $\alpha_M = 0^\circ$, $\alpha_A = 6^\circ$ and $k = 0.14$

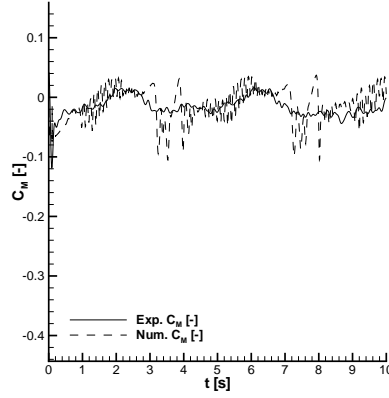


Figure 19 Pitching moment coefficient from experimental and numerical data for $\alpha_M = 0^\circ$, $\alpha_A = 6^\circ$ and $k = 0.14$

and 21 show a similar situation as described for the fixed angle of attack. The triple vortex structure and especially the primary vortex situated at the trailing edge is represented properly in the numerical simulation. In Fig. 22 the separation bubbles at the leading and trailing edge can be identified, but their structure is not clearly visible in Fig. 23 due to the optical overlapping of the airfoil front edge. Nevertheless it is clear that separation occurs.

4 Results

4.1 Influence of the Reduced Frequency on the Aerodynamic Coefficients

As shown in the literature [19, 3, 18, 17] both the reduced frequency:

$$k = \frac{\pi f c}{u_\infty}, \quad (13)$$

and the non-dimensional pitching rate:

$$\alpha_+ = \frac{\dot{\alpha} c}{u_\infty} = \frac{2\pi f c \alpha_A}{u_\infty} \cos(2\pi f(t - t_{osc})) = 2k\alpha_A \cos(2\pi f(t - t_{osc})), \quad (14)$$

are the dominant parameters, which influence the unsteady aerodynamic coefficients of an oscillating airfoil. These influences are to be discussed in the

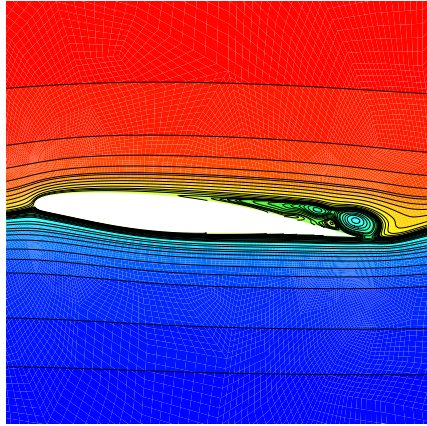


Figure 20 Numerical instantaneous streamlines at $\alpha = 5.9^\circ \downarrow$ and $t = 5.208 \text{ s}$ for $\alpha_M = 0^\circ$, $\alpha_A = 6^\circ$ and $k = 0.14 \text{ Hz}$

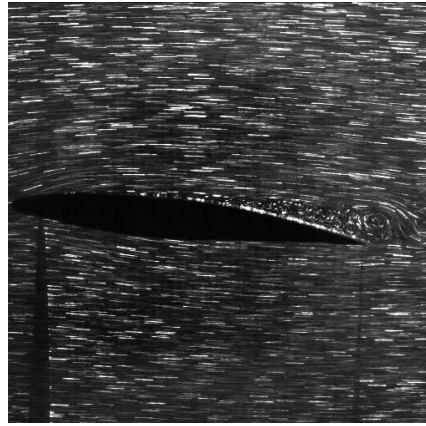


Figure 21 Experimental particle visualization at $\alpha = 5.9^\circ \downarrow$ and $t = 5.201 \text{ s}$ for $\alpha_M = 0^\circ$, $\alpha_A = 6^\circ$ and $k = 0.14 \text{ Hz}$

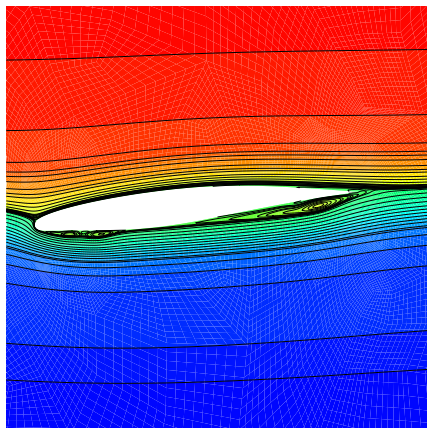


Figure 22 Numerical instantaneous streamlines at $\alpha = -5.8^\circ \downarrow$ and $t = 6.911 \text{ s}$ for $\alpha_M = 0^\circ$, $\alpha_A = 6^\circ$ and $k = 0.14 \text{ Hz}$

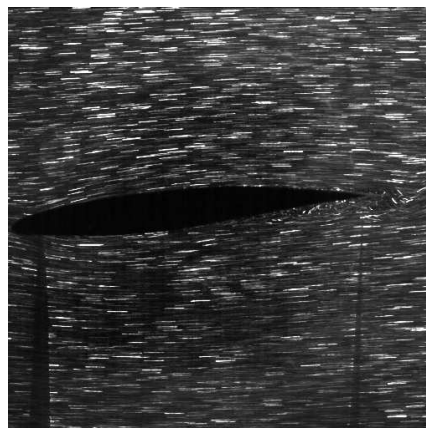


Figure 23 Experimental particle visualization at $\alpha = -5.8^\circ \downarrow$ and $t = 6.901 \text{ s}$ for $\alpha_M = 0^\circ$, $\alpha_A = 6^\circ$ and $k = 0.14 \text{ Hz}$

reduced frequency range of 0 to 0.28.

The following figures show the influence of the reduced frequency on the aerodynamic coefficients at an instantaneous pitching rate of $\alpha_+ = 0$, which corresponds to the peak values at $\alpha_A = \alpha = 6^\circ$. In Fig. 24 no significant influence of the reduced frequency can be detected for the range of reduced frequencies investigated. The lift stays constant at approximately the static value. This behaviour can be observed for both experimental series, as well as for the numerical data, which coincides well. The variation in the static lift coefficient for $\alpha_A = 6^\circ$ is of experimental nature and is attributed to three-dimensional unsteady effects in the test section. For the drag coefficient at $\alpha_A = 6^\circ$, a gradual decrease can be observed up to $k = 0.14$ (see Fig. 25). From $k = 0.14$ to 0.28 the drag is constant. For $\alpha_A = 3^\circ$ the drag seems to be constant for the whole range of reduced frequencies. In the numerical simulations a lower drag coefficient is calculated, although the tendencies are equal. The numerical and experimental absolute pitching moment for $\alpha_A = 3^\circ$ shows at first an increase and then slight decrease with greater reduced frequencies (see Fig. 26). For $\alpha_A = 6^\circ$ the absolute experimental values show a gradual increase with frequency from $k = 0.14$ onwards, while the numerical data seems to reach a constant value. Experimental and numerical data is equal in this case for $k = 0.28$. Further numerical simulations are needed to confirm the results and detect a tendency. It must be emphasized that the pitching moment is very sensitive and is strongly influenced by the reduced frequency, far more than the lift or drag coefficients.

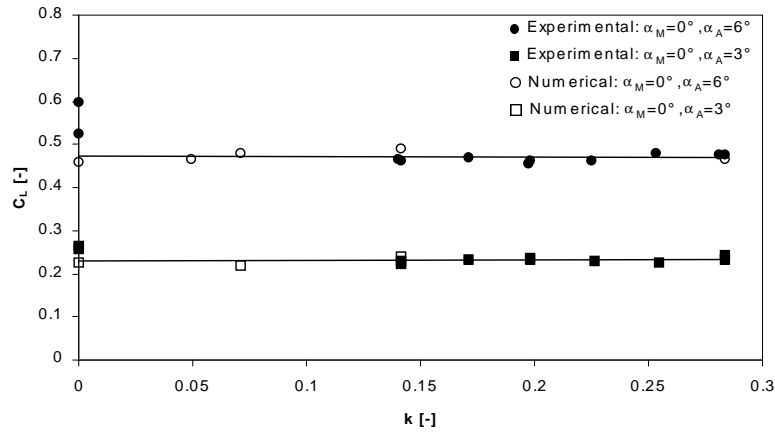


Figure 24 Numerical and experimental lift coefficient at $\alpha_A = 3^\circ$ and 6° as a function of the reduced frequency

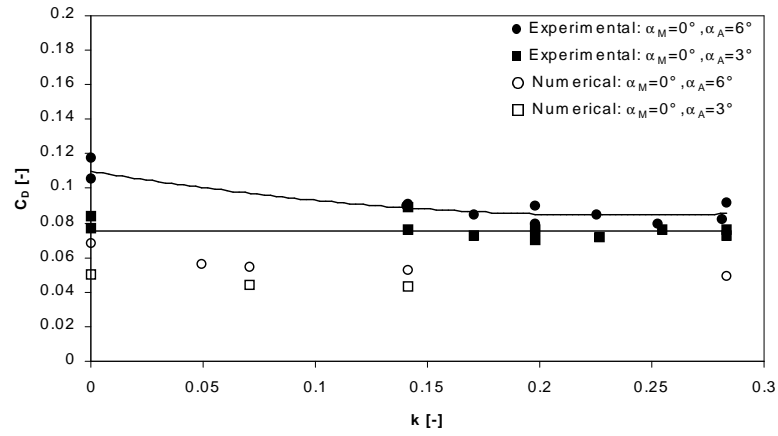


Figure 25 Numerical and experimental drag coefficient at $\alpha_A = 3^\circ$ and 6° as a function of the reduced frequency

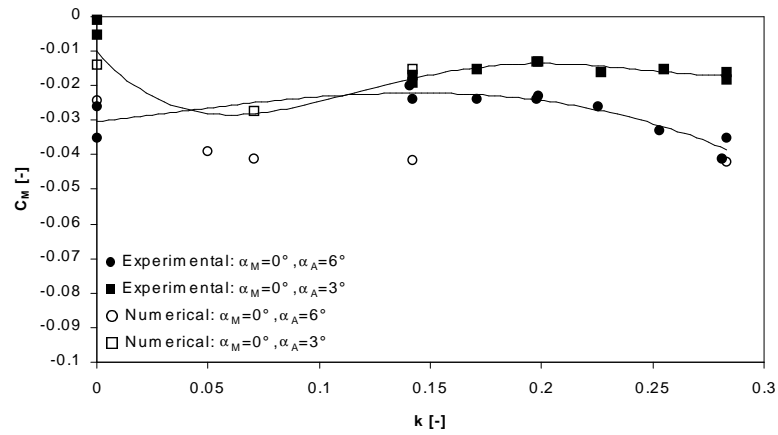


Figure 26 Numerical and experimental pitching moment coefficient at $\alpha_A = 3^\circ$ and 6° as a function of the reduced frequency

4.2 Influence of the Pitching Rate on the Aerodynamic Coefficients

Figures 27 and 28 show the influence of the instantaneous positive pitching rate at $\alpha = 3^\circ$ for $\alpha_A = 6^\circ$ in comparison with the peak values for the same angle of attack, hence $\alpha_A = 3^\circ$ and $\alpha_+ = 0$. For the lift and the pitching moment coefficient, dynamic effects are apparent. The lift is increased in comparison to the $\alpha_+ = 0$ values. Here the experimental data shows a greater gain in lift than the numerical data. The tendency with increasing pitching rate is equal in both data sets. For the pitching moment the results are not quite clear. For greater reduced frequencies $k > 0.14$ the absolute value is slightly increased, while the numerical data for $k = 0.07$ is smaller than the corresponding value at $\alpha_A = 3^\circ$. Overall a positive non-dimensional pitching rate increases the lift, which corresponds to results presented by other researchers [17, 18] for large angles of attacks.

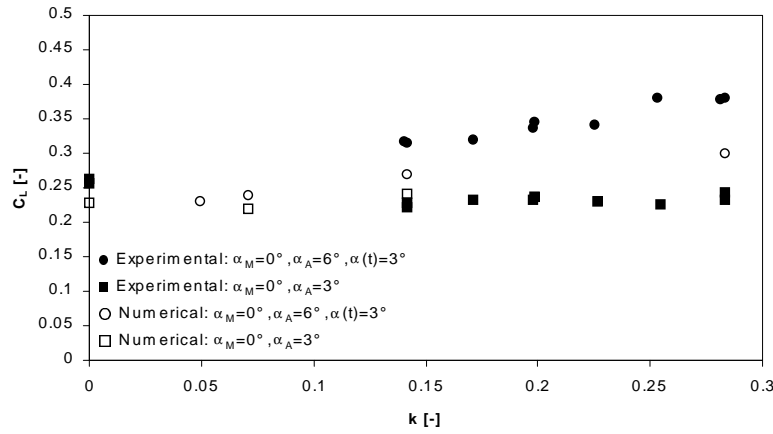


Figure 27 Influence of the non-dimensional pitching rate at $\alpha_+ = \sqrt{3}k\alpha_A$ for $\alpha_A = 6^\circ$ and $\alpha_+ = 0$ for $\alpha_A = 3^\circ$ on the lift coefficient

4.3 Hysteresis of the Lift and Pitching Moment Coefficient Hysteresis Loops

Figures 29 to 32 show the lift and pitching moment coefficients plotted against the instantaneous angle of attack. With increasing reduced frequency the phase difference between the aerodynamic coefficients and the airfoil motion becomes apparent. In Fig. 29 the lift values show no hysteresis for large positive angles of attack. The lift travels along a straight line, even though trailing edge separation occurs. For a negative angle of attack a strong influ-

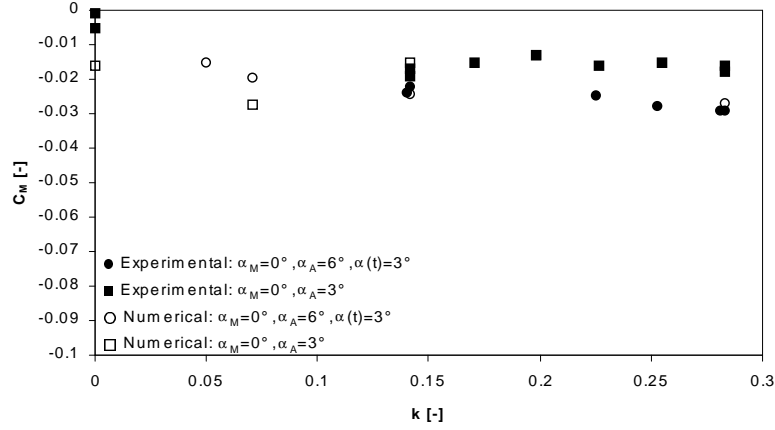


Figure 28 Influence of the non-dimensional pitching rate at $\alpha_+ = \sqrt{3}k\alpha_A$ for $\alpha_A = 6^\circ$ and $\alpha_+ = 0$ for $\alpha_A = 3^\circ$ on the pitching moment coefficient

ence of the leading and trailing edge separation occurring on the lower side of the airfoil can be seen (see Fig. 23), creating large fluctuations in the lift coefficient. The separation grows once the airfoil pitches up and vanishes when a positive angle of attack of about $\alpha = 3^\circ$ is reached. In contrast in Fig. 31 for higher reduced frequencies a hysteresis can be observed from $k = 0.14$ onwards. The effect is also evident in the pitching moment in Figs. 30 and 32. For an angle of attack between $\alpha = 0^\circ$ and -6° fluctuations are observed for $k < 0.28$ and a peak value in the range of $\alpha = 0^\circ$ to -2° for $k = 0.14$ and 0.28 . The fluctuations disappear for $k = 0.28$, where the pitching moment decreases gradually from the value at $\alpha = -6^\circ$ to a peak at -2° . Vortex shedding on the lower side of the airfoil is suppressed in this case. At this reduced frequency $k = 0.28$, steady separation phenomena are strongly influenced by the motion of the airfoil.

4.4 Trailing Edge Separation on the Pitching BAC3-11/RES/30/21 Airfoil

The Figs. 33 to 38 present the evolution of the flow in the pitching up phase of one oscillation cycle. During the pitching up manoeuvre, the separation on the lower side of the airfoil vanishes and a new separation bubble establishes itself on the upper side near to the trailing edge. The effects of the lower side separation bubble where shown in Sec. 4.3. Unfortunately the experimental data in Fig. 33 does not show the lower side separation bubble seen in the numerical data. The reason is that the front profile edges of the airfoil cover areas near to the airfoil due to the optical arrangement. The separation on

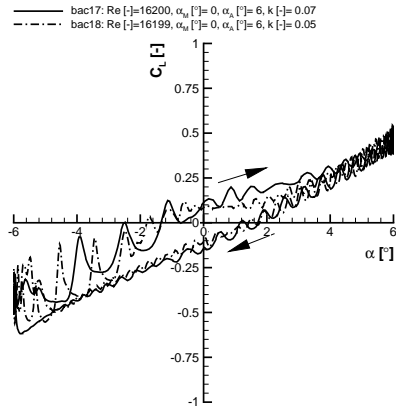


Figure 29 Lift coefficient plotted versus angle of attack for $\alpha_M = 0^\circ$, $\alpha_A = 6^\circ$, $k = 0.05$ and $k = 0.07$

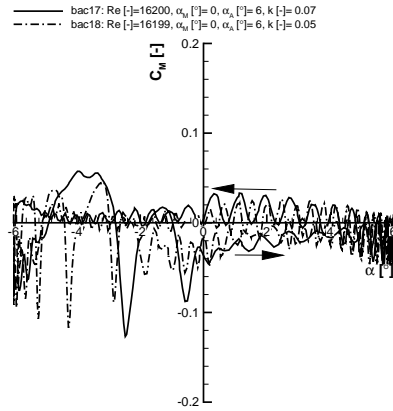


Figure 30 Pitching moment coefficient plotted versus angle of attack for $\alpha_M = 0^\circ$, $\alpha_A = 6^\circ$, $k = 0.05$ and $k = 0.07$

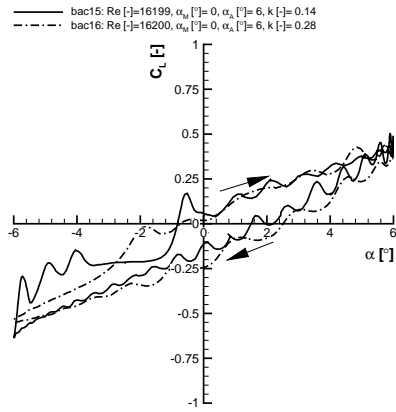


Figure 31 Lift coefficient plotted versus angle of attack for $\alpha_M = 0^\circ$, $\alpha_A = 6^\circ$, $k = 0.14$ and $k = 0.28$

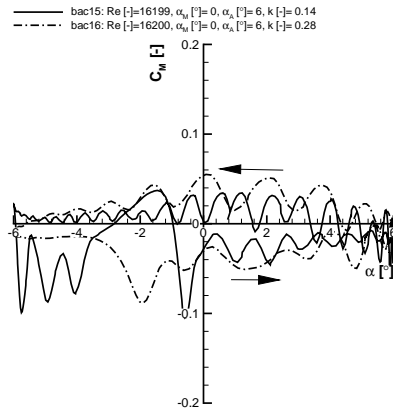


Figure 32 Pitching moment coefficient plotted versus angle of attack for $\alpha_M = 0^\circ$, $\alpha_A = 6^\circ$, $k = 0.14$ and $k = 0.28$

the upper side is started by a flow reversal region, with a primary clockwise vortex developing (see Fig. 36). The primary vortex induces the growth of a counterclockwise secondary vortex, which again stimulates the creation of third clockwise vortex. This triple vortex system grows as seen in Fig. 38 until the primary vortex is shed into the wake. This process is repeated periodically. It must be emphasized that the same process takes place at a static angle, where vortices are shed at about a frequency of 10 Hz into the wake (see Fig. 15). For the oscillating airfoil the separation is usually smaller. This becomes obvious comparing Figs. 15 and 37 or 14 and 38.

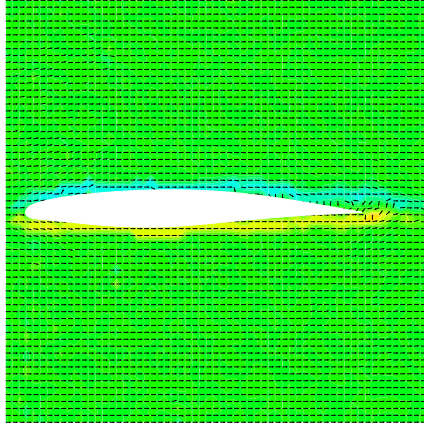


Figure 33 Experimental velocity vectors and vorticity for $\alpha_M = 0^\circ$, $\alpha_A = 6^\circ$ and $k = 0.14$ at $\alpha = 0^\circ$ and $t = 4.1\text{ s}$

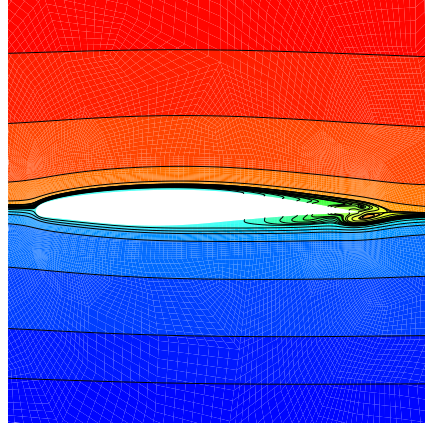


Figure 34 Numerical streamlines for $\alpha_M = 0^\circ$, $\alpha_A = 6^\circ$ and $k = 0.14$ at $\alpha = 0.2^\circ$ and $t = 4.108\text{ s}$

5 Conclusions

In the context of this project both experimental and numerical tools have been developed, which allow the study of flow fields around oscillating airfoils for various kinematic and geometric parameters in an acceptable amount of time. The numerical tool has been successfully verified with experiments and allows a time efficient computation of cases which cannot be run in the experimental facility and thus enhances the experimental data very well. This combination is very promising for this kind of investigation, despite the fact of the relatively high Reynolds number and different space dimensions. Promising results are presented, showing the primary influence of two well known parameters, the reduced frequency and the non-dimensional pitching rate, for two amplitude angles of attack of $\alpha_A = 3^\circ, 6^\circ$ and for a relevant range of reduced frequencies for the reference airfoil BAC3-11/RES/30/21.

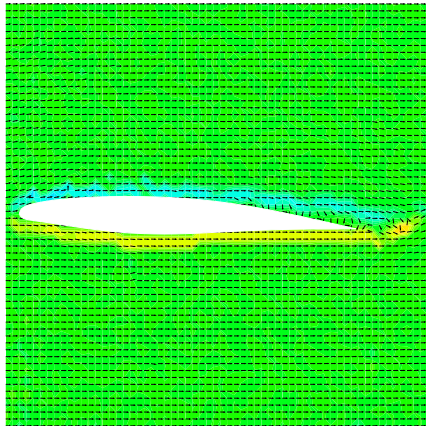


Figure 35 Experimental velocity vectors and vorticity for $\alpha_M = 0^\circ$, $\alpha_A = 6^\circ$ and $k = 0.14$ at $\alpha = 2.7^\circ$ and $t = 4.4$ s

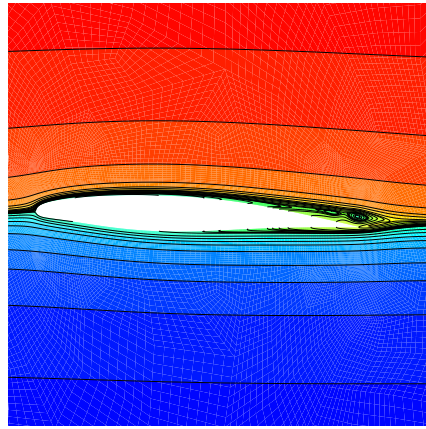


Figure 36 Numerical streamlines for $\alpha_M = 0^\circ$, $\alpha_A = 6^\circ$ and $k = 0.14$ at $\alpha = 2.9^\circ$ and $t = 4.408$ s

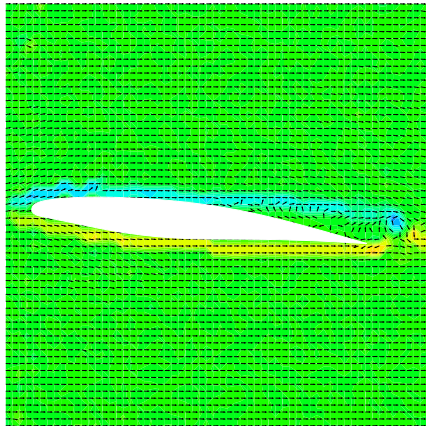


Figure 37 Experimental velocity vectors and vorticity for $\alpha_M = 0^\circ$, $\alpha_A = 6^\circ$ and $k = 0.14$ at $\alpha = 5.9^\circ$ and $t = 5$ s

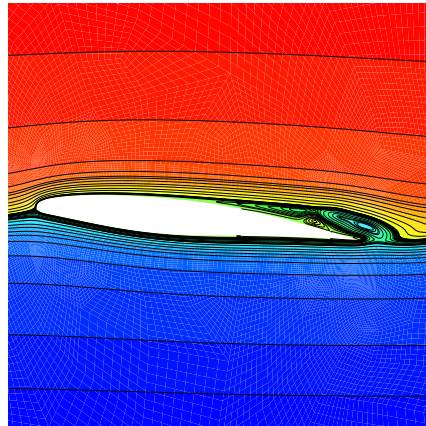


Figure 38 Numerical streamlines for $\alpha_M = 0^\circ$, $\alpha_A = 6^\circ$ and $k = 0.14$ at $\alpha = 6^\circ$ and $t = 5$ s

An increasing reduced frequency has little effect on the peak values of the aerodynamic coefficients, while the flow field is gradually affected. The non-dimensional pitching rate influences the aerodynamic coefficients, which for positive values results in an increase in lift. The flow field due to the motion of the airfoil is overlaid by separation regions of the type encountered at a static angle of attack and are influenced by the unsteady motion. Further investigation is required in order to complete the study for many variations of the kinematic and geometric parameters. The same experiments have been already conducted for other airfoil models and it will be interesting to discover the differences arising.

References

- [1] BENNET, R. M.; EDWARDS, J. W.: *An Overview of Recent Developments in Computational Aeroelasticity*. AIAA Paper 1998-2421, 29th Fluid Dynamics Conference, Albuquerque, NM (1998)
- [2] KUMAR, A.; HEFNER, J.: *Future Challenges and Opportunities in Aerodynamics*. ICAS 2000-0.2.1, ICAS 2000 Congress (2000)
- [3] MCCROSKEY, W. J.: *Unsteady Airfoils*. Ann. Rev. Fluid Mechanics, Vol. 14, pp. 285-311 (1982)
- [4] AKAMATSU, T.: *Application of shock tube technology to studies of hydrodynamics*. Shock Tube and Shock Wave Research (ed. Ahlborn, Herzberg, Russel), University of Washington Press, Seattle and London, (1978)
- [5] WERNERT, P.; FAVIER, D.: *Considerations about the phase averaging method with application to ELDV and PIV measurements over pitching airfoils*. Experiments in Fluids 27, p. 473-483, Springer-Verlag (1999).
- [6] WERNERT, P.; KOERBER, G.; WIETRICH, F. ET AL.: *Demonstration by PIV of the Non-Reproduceability of the Flow Field Around an Airfoil Pitching Under Deep Dynamic Stall Conditions and Consequences Thereof*. Aerospace Science and Technology, Vol. 2, p. 125-135, (1997).
- [7] ADRIAN, A. J.: *Particle-Image Techniques for Experimental Fluid Mechanics*. Annual Review of Fluid Mechanics, Vol. 23, p. 261-304 (1991).
- [8] WEIGAND, A.: *Review of some Novel Measurement Techniques for Fluid Dynamics Studies*. DGLR Jahrestagung, Göttingen, Germany (1993).
- [9] WILLERT, C. E.; GHARIB, M.: *Digital particle image velocimetry*. Experiment in Fluids 10, p. 181-193, (1991).

- [10] SHAND, A. M.: *The Investigation, Development and Optimisation of Global Laser Diagnostics for Combustion and Related Flow Applications*. PhD Thesis, University of Warwick, (1996).
- [11] TUREK, S.; BECKER, C.: *FEATFLOW. Finite element software for the incompressible Navier-Stokes equations. User Manual. Release 1.1*. Technical Report, University of Heidelberg, Germany (1998).
- [12] TUREK, S.: *Efficient solvers for incompressible flow problems: An algorithmic approach in view of computational aspects*. LNCSE 6, Springer Verlag (1999).
- [13] SCHÄFER, M; TUREK, S.: *Benchmark Computations of Laminar Flow Around a Cylinder*. In: Flow Simulation with High-Performance Computers II, Ed. Hirschel, E. H., NNFM Vol. 52, Vieweg Verlag (1996).
- [14] HESSE, M.; BRITTEN, G.; BALLMANN, J.: *A Multi-Block Grid Deformation Algorithm for Aeroelastic Analysis*. Lehr- und Forschungsgebiet für Mechanik, RWTH Aachen, Not yet published (2000).
- [15] WALL, W. A.: *Fluid structure interaction with stabilized finite elements*. Institute of Structural Mechanics, University of Stuttgart, PhD Thesis (1999).
- [16] WAGNER, R.: *Numerical Simulation of Selective Water-Ludwig-Tunnel Experiments*. Student Thesis, Shock Wave Laboratory, RWTH Aachen (2000).
- [17] OHMI, K.; COUTANCEAU, M.; LOC, T. ET AL.: *Vortex formation around an oscillating and translating airfoil at large incidences*. J. Fluid Mechanics, Vol. 211, pp. 37-60 (1990).
- [18] WALKER, J. M.; HELIN, H. E.; STRICKLAND, J. H.: *An Experimental Investigation of an Airfoil Undergoing Large-Amplitude Pitching Motions*. AIAA Journal, Vol. 23, No. 8, pp. 1141-1142 (1985).
- [19] THEODORSEN, T.: *General theory of aerodynamic instability and the mechanism of flutter*. NACA Report 496 (1935).